Single atomic Co decorated mesoporous carbon/MXene heterostructure as redox promoters for high-stable Li–S battery

Jiaheng Bao [a], Xiang Li [a], Tao Rong [a], Jian Wang [b,c,d,*], Jianan Gu [e], Xiaomin Cheng [b], Yanli Wang [a,**], Hongzhen Lin [b], Liang Cheng [a,***], Liang Zhan [a], Yongzheng Zhang [a,****]

[a] *State Key Laboratory of Green Chemical Engineering and Industrial Catalysis, State Key Laboratory of Chemical Engineering, Key Laboratory of Specially Functional Polymeric Materials and Related Technology (Ministry of Education), Shanghai Key Laboratory of Multiphase Materials Chemical Engineering, East China University of Science and Technology, Shanghai, 200237, China*
[b] *I-Lab & CAS Key Laboratory of Nanophotonic Materials and Device, Suzhou Institute of Nano-Tech and Nano-Bionics, Chinese Academy of Sciences, Suzhou, 215123, China*
[c] *Helmholtz Institute Ulm (HIU), D89081 Ulm, Germany*
[d] *Karlsruhe Institute of Technology (KIT), D76021 Karlsruhe, Germany*
[e] *State Key Laboratory of Alternate Electrical Power System with Renewable Energy Sources, School of New Energy, North China Electric Power University, 100096, Beijing, China*

Keywords:
MXene
Mesoporous carbon
Single-atom catalyst
Sulfur conversion
Lithium-sulfur batteries

ABSTRACT

Lithium-sulfur (Li–S) batteries are considered a potential breakthrough in future energy storage systems owing to remarkable energy density. However, they are fundamentally constrained by practical obstacles including polysulfide shuttle effect and sluggish redox reaction kinetics. To address these challenges, single atomic Co decorated sandwich-like mesoporous carbon/MXene heterostructure (SACo-MC@MX) is designed by using a single-micelle-directed interfacial assembly strategy. This innovative catalytic heterostructure is endowed with combined physical adsorption and chemical anchoring capability toward effectively capturing lithium polysulfides, while simultaneously enhancing the redox reaction kinetics of sulfur species through Co atomic catalysis, as fully confirmed by comprehensive electrochemical characterizations and in-situ Raman. The cell employed with SACo-MC@MX achieves an impressive capacity of 1241.6 mAh g^{-1} at 0.2C, an excellent rate capability up to 5C, and outstanding long-term cycling stability with a low decay rate of 0.030 % per cycle at 1C over 1000 cycles. Additionally, even with a high sulfur loading of 5.3 mg cm^{-2}, the cell retains a superior areal capacity of 4.64 mAh cm^{-2} after 100 cycles, providing the possibility to commercialize Li–S batteries.

1. Introduction

To deal with global energy shortage and worsening ecological challenges, energy storage devices, as a key part of renewable energy systems, have drawn significant attention from researchers [1–3]. Lithium-sulfur (Li–S) batteries are broadly recognized as competitive contenders for modern power storage solutions owing to their impressive theoretical energy density and capacity (2600 Wh kg^{-1}/1675 mAh g^{-1}), economic viability, and ecological sustainability [4–6]. However, several obstacles impede the commercial realization of Li–S batteries due to the complex multi-electron redox reactions between solid and liquid active phases, leading to the shuttle effect of lithium polysulfides (LiPSs) and sluggish redox kinetics [7,8]. These issues collectively undermine the electrochemical performance of Li–S batteries, causing rapid capacity fading and inferior rate capabilities [9–11].

To tackle these obstacles, various approaches have been explored, including the construction of conductive sulfur hosts [12–14], the design of functional separators [15–17] and the optimization of electrolytes [18–20]. Among them, developing functional separators has been identified as one of the simplest and most effective methods [21].

---

* Corresponding author. Helmholtz Institute Ulm (HIU), D89081 Ulm, Germany.
** Corresponding author.
*** Corresponding author.
**** Corresponding author.
E-mail addresses: wangjian2014@sinano.ac.cn, jian.wang@kit.edu (J. Wang), ylwang@ecust.edu.cn (Y. Wang), chengliang@ecust.edu.cn (L. Cheng), zhangyongzheng@ecust.edu.cn (Y. Zhang).

Separator coatings with the functions of physical confinement and chemical anchoring capabilities can efficiently trap soluble LiPSs, mitigate the shuttle effect, and redistribute active sulfur species, significantly improving the sulfur utilization [22,23]. Furthermore, introducing catalysts into the coatings can strengthen LiPSs conversion, ultimately improving the rate capability of Li–S batteries [24,25]. MXene, as an emerging 2D transition metal carbide/nitride, has demonstrated exceptional advantages in energy storage applications owing to its electrochemical stability, superior electrical conductivity, and Lewis site modulation [26,27]. In addition, compared to traditional 2D materials, MXene offers abundant functional groups (-O, –OH and –F) that provide active sites for LiPSs adsorption [28]. It should be noted that MXene nanosheets exhibit a tendency to restacking because of van der Waals forces and hydrogen bonding, limiting functional surface accessibility and ion transport [29]. In this case, heterostructure engineering that incorporates nanomaterials onto MXene has been proposed as a promising solution [30–32]. Our previous work has demonstrated that grafting ordered mesoporous carbon onto MXene can effectively prevent MXene stacking and create pathways to boost ion diffusion [33]. However, the limited active catalytic sites in the mesoporous carbon/MXene heterostructure limit its catalytic performance, particularly under high concentrations of LiPSs, necessitating further catalytic enhancement.

Recently, single-atom catalysts (SACs) have emerged as superior candidates for energy conversion, attributed to their nearly 100 % atomic utilization and unique electronic properties [34,35], which has been demonstrated the feasibility in Li–S batteries [36–39]. SACs can effectively alleviate the shuttle effect of LiPSs through polar interactions, while the densely exposed metal centers enable efficient bidirectional catalysis of polysulfide intermediates [40]. Given that, a single atomic Co decorated sandwich-like mesoporous carbon/MXene heterostructure (SACo-MC@MX) was achieved by using a single-micelle-directed interfacial assembly strategy. In this design, the mesoporous carbon was uniformly grafted onto both surfaces of the MXene nanosheets to prevent restacking, offering a robust framework for efficient electron and ion transport. Meanwhile, the exposed Lewis acidic sites facilitated the capture of LiPSs and the Co single atoms exhibited strong catalytic activity, realizing the goal of "adsorption-catalysis-transformation". As a result, the SACo-MC@MX enables Li–S cells to obtain remarkable rate performance (716.7 mAh g^{-1} at 5C) and long cycle life (capacity degradation of 0.030 % per cycle at 1C over 1000 cycles). Impressively, even with a high sulfur loading of 5.3 mg cm^{-2}, the cell retains a superior capacity of 4.64 mAh cm^{-2} after 100 cycles, exhibiting the potential application in practical demands.

2. Experimental section

2.1. Synthesis of MXene

The MXene (Ti_3C_2) nanosheets were synthesized following a procedure adapted from previously reported methods [41]. Briefly, 4.8 g of LiF was dissolved in a solution containing 45 mL of HCl and 15 mL of H_2O. After stirring for 10 min, 2.0 g of MAX phase (Ti_3AlC_2) was introduced, and the reaction was maintained at 35 °C for 24 h. The final product was thoroughly washed with deionized water until the pH reached neutrality (~7.0). Finally, a 1.5 mg mL^{-1} MXene nanosheet dispersion was prepared and refrigerated for storage.

2.2. Synthesis of SACo-MC@MX

To synthesize SACo-MC@MX, 1 g of F127 was dissolved in 50 mL ethanol, and then the 50 mL MXene dispersion, 1 g dopamine hydrochloride, 50 mg $Co(NO_3)_2\cdot 6H_2O$, and 3 mL 1,3,5-Trimethylbenzene were added in sequence. After stirring for 30 min, 2.5 mL $NH_3\cdot H_2O$ was introduced, and the mixture was stirred for 8 h. The product was repeatedly washed via centrifugation with deionized water and ethanol, then dried at 50 °C for 12h. The precursor was carbonized under a nitrogen atmosphere by heating it at 800 °C for 2 h. The final product was subjected to 2 M HCl treatment for 10 h to obtain SACo-MC@MX. For MC@MX, the identical procedure was followed without adding $Co(NO_3)_2\cdot 6H_2O$.

3. Results and discussion

The synthesis process of SACo-MC@MX is illustrated in Fig. 1a. Under mild conditions, Ti_3C_2 MXene nanosheets were synthesized by selectively etching the Al atomic layer from Ti_3AlC_2 MAX using HCl and LiF. Subsequently, Co-PDA/F127 micelles were uniformly self-assembled onto both surfaces of MXene through electrostatic interactions and hydrogen bonding. After carbonization and acid washing, single atomic Co decorated sandwich-like mesoporous carbon/MXene heterostructure (SACo-MC@MX) was obtained.

Transmission electron microscopy (TEM) images (Fig. S1) revealed that the etched Ti_3C_2 MXene displayed an ultra-thin and sheet-like morphology. As shown in the scanning electron microscopy (SEM) images (Figs. 1b and S2a), SACo-MC@MX and MC@MX both retained the original 2D morphology of MXene. Moreover, both sides of the materials displayed highly uniform and continuously open mesopores, indicating the successful grafting of mesoporous carbon onto the MXene surfaces, leading to the formation of a sandwich-like structure. This unique heterostructure provides effective pathways for electron transfer and Li^+ diffusion. TEM images (Figs. 1c and S2b) further confirmed the 2D morphology of SACo-MC@MX and MC@MX, with orderly arranged mesopores, some of which were overlapping, providing additional evidence that mesoporous carbon was located on both sides of the MXene sheets. Furthermore, no noticeable Co metal nanoparticles were detected in the TEM images of SACo-MC@MX. Elemental mapping images (Fig. 1e) showed a uniform distribution of C, N, Ti, and Co elements without any aggregation, suggesting that Co atoms in SACo-MC@MX might exist in an atomic-scale form. To investigate the exact form of the Co element, aberration-corrected TEM (AC-TEM) analysis was conducted. As shown in Fig. 1d, numerous randomly dispersed bright spots were observed on the surface of SACo-MC@MX, verifying that Co is present as single atoms on the mesoporous carbon surface.

X-ray diffraction (XRD) analysis was performed to analyze the crystalline phase structure of SACo-MC@MX and its synthetic precursors. As shown in Fig. S3, after etching the Ti_3AlC_2 MAX phase with the HCl and LiF solution, the Al-related diffraction peak at $2\theta = 39°$ disappeared, while the 002 diffraction peak shifted from $2\theta = 9.5°$ to 6.4°. This shift in the 002 diffraction peak indicates an increase in interlayer spacing caused by the exfoliation effect, suggesting the formation of thinner Ti_3C_2 MXene layers with fewer layers [42]. From the XRD patterns of SACo-MC@MX and MC@MX (Fig. 2a), it is evident that the characteristic MXene diffraction peak at $2\theta = 6.4°$ vanished, being replaced by a broad peak at $2\theta = 25.5°$, corresponding to the 002 diffraction peak of disordered carbon structures. This result confirms the successful formation of mesoporous carbon on the MXene surfaces. Additionally, no Co-related diffraction peaks were observed, indicating the absence of Co metal particles in SACo-MC@MX. Furthermore, the XRD patterns of SACo-MC@MX and MC@MX are nearly identical, suggesting that the presence of Co atoms has minimal impact on the overall structure. The specific surface area and pore structure of the materials were analyzed using nitrogen adsorption–desorption isothermal curves (Fig. 2b). SACo-MC@MX displays typical type IV isotherms with distinct hysteresis loops, characteristic of mesoporous structures. The BET surface area of SACo-MC@MX is 330.2 $m^2\ g^{-1}$, substantially higher than that of original MXene nanosheets (22.5 $m^2\ g^{-1}$). This increase demonstrates that the formation of mesoporous carbon on MXene effectively inhibits the restacking of the 2D layers and introduces abundant porosity. The pore size distribution (Fig. 2c) reveals that SACo-MC@MX has average pore sizes of 3.82 nm, further confirming the mesoporous nature. The extensive surface area and mesoporous structure effectively

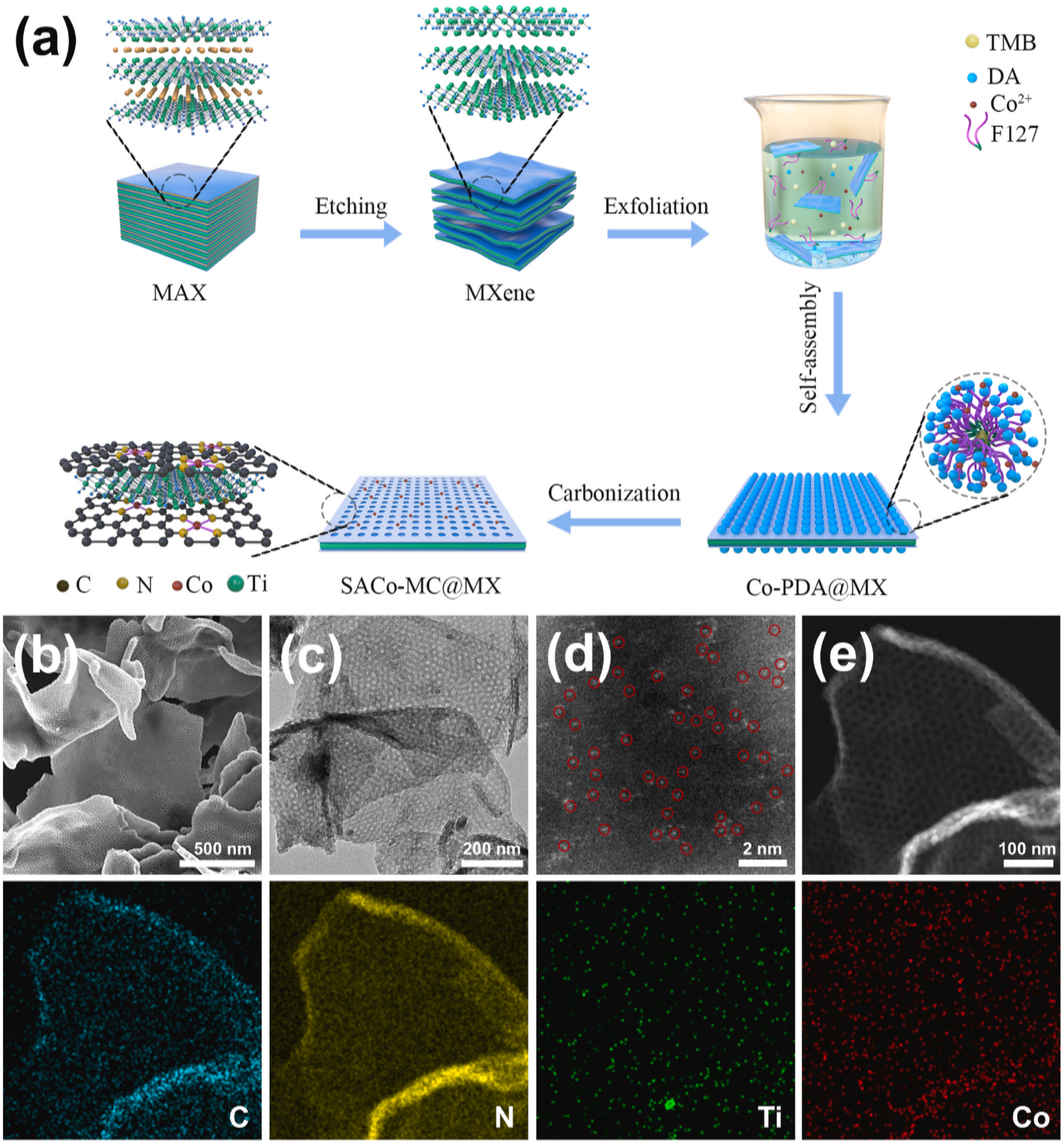

Fig. 1. (A) Schematic illustration of the synthesis process of SACo-MC@MX. (b) SEM image, (c) TEM image, and (d) AC-TEM image of SACo-MC@MX. (e) Element mapping images of the SACo-MC@MX.

expose additional active sites for LiPSs catalytic conversion, while providing cross-plane channels for ion transport, thereby enhancing electrolyte infiltration and accelerating ion diffusion to promote the sulfur redox reaction [43].

As shown in the Raman spectra (Fig. 2d), both SACo-MC@MX and MC@MX exhibit two prominent characteristic peaks near 1350 cm^{-1} and 1580 cm^{-1}, corresponding to the D-band and G-band of mesoporous carbon [44]. The I_D/I_G ratios of SACo-MC@MX and MC@MX are 1.10 and 1.16, indicating that both materials possess good graphitization. The surface chemistry of SACo-MC@MX was further investigated by X-ray photoelectron spectroscopy (XPS) analysis. As shown in Fig. S4a, the presence of the C–N bond indicates successful N doping in the mesoporous carbon, which introduces additional polar sites for LiPSs adsorption, thereby suppressing the shuttle effect [45]. The N 1s spectrum (Fig. 2e) reveals four distinct peaks at binding energies of 389.5, 400.7, 401.5, and 404.4 eV, corresponding to pyridinic N, pyrrolic N, graphitic N, and oxidized N. Pyrrolic N and pyridinic N can act as coordination sites for Co atoms, facilitating the coordination of Co single atoms [46]. The Co 2p spectrum (Fig. 2f) shows relatively noisy data, indicating a low Co content in SACo-MC@MX. The fitted peaks at 779.6 and 794.2 eV correspond to Co^{3+}, while those at 781.9 and 797.2 eV correspond to Co^{2+}. Satellite peaks at 786.2 and 803.4 eV are also observed. Notably, no peak is detected at 778.2 eV, indicating the absence of metallic Co clusters [47]. The Ti 2p spectrum (Fig. S4b) exhibits fitted peaks at 457.0 and 463.0 eV, corresponding to Ti–C bonds, while peaks at 459.2 and 464.4 eV are attributed to C–Ti–O bonds. Additionally, the peaks at 459.8 and 465.6 eV correspond to Ti–O bonds [48]. These functional groups confirm the presence of MXene, and the appearance of Ti–O bonds indicates slight oxidation of MXene.

To investigate the adsorption capacity of SACo-MC@MX for LiPSs, Li_2S_6 adsorption experiments were conducted. As shown in the inset of Fig. 3a, equal masses of SACo-MC@MX and MC@MX were immersed in

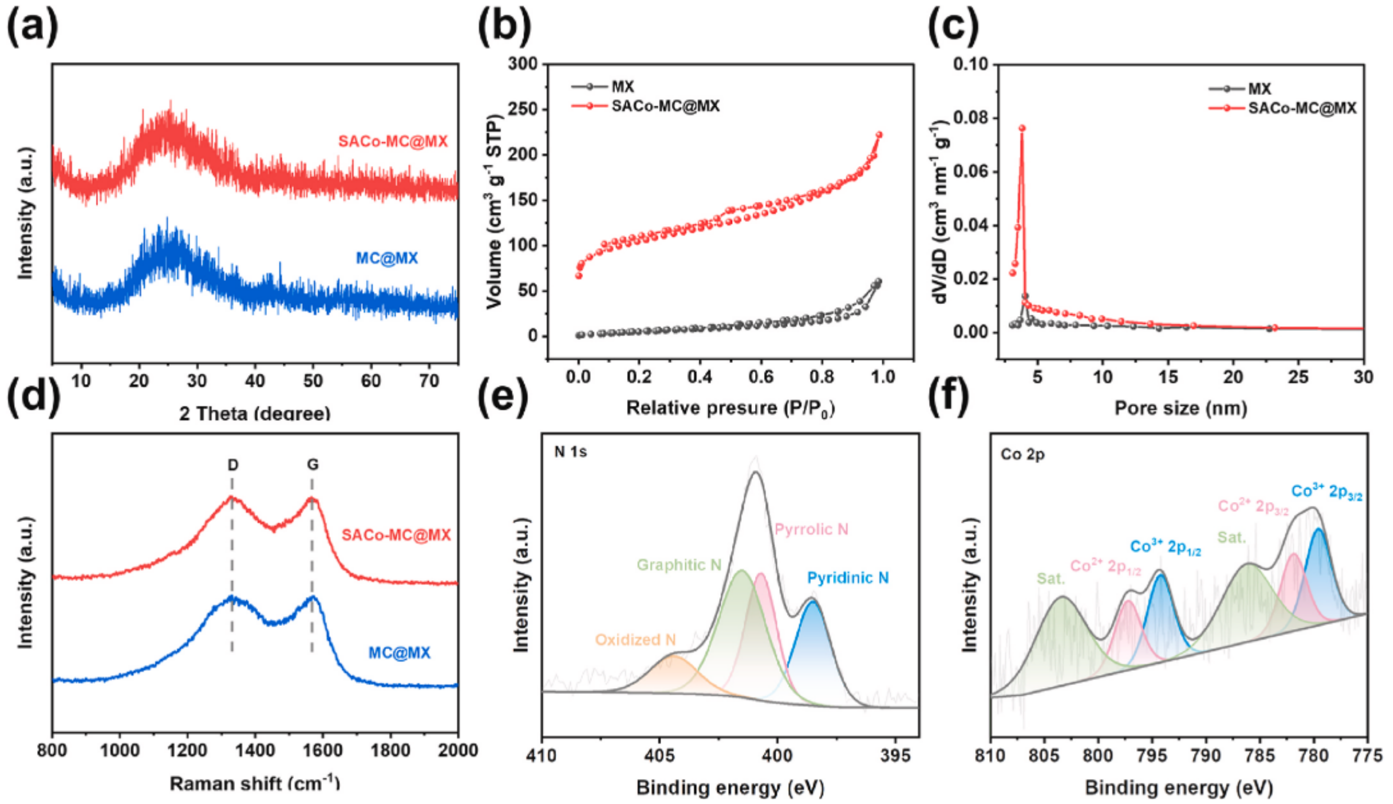

Fig. 2. (A) XRD patterns of SACo-MC@MX and MC@MX. (b) N_2 adsorption–desorption isotherms curves, and (c) corresponding pore size distributions of SACo-MC@MX and MX. (d) Raman spectra of SACo-MC@MX and MC@MX. (e) N 1s and (f) Co 2p XPS spectra of SACo-MC@MX.

2 mM Li_2S_6 solution. After standing for 12 h, both SACo-MC@MX and MC@MX showed significant decolorization of the Li_2S_6 solution compared to the blank, indicating strong adsorption of Li_2S_6. The incorporation of mesoporous carbon provided additional adsorption sites, while SACo-MC@MX exhibited superior adsorption performance, with the supernatant becoming nearly colorless and transparent. Subsequently, UV–vis spectroscopy was performed on the supernatants to quantify the residual Li_2S_6. As shown in Fig. 3a, the SACo-MC@MX system exhibited the lowest absorption intensity, demonstrating that Co single atoms markedly enhanced the chemical anchoring of polysulfides. This improved anchoring suppresses the polysulfide shuttle effect, thereby enhancing battery capacity retention and cycle life [49].

To further explore the interactions between SACo-MC@MX and LiPSs, SACo-MC@MX before and after Li_2S_6 adsorption were characterized. In the Li 1s spectrum (Fig. 3b), two fitted peaks at 55.2 and 56.3 eV correspond to Li–S and Li–N bonds, indicating that the abundant N-doped polar sites in SACo-MC@MX effectively anchored LiPSs and suppressed the shuttle effect [50]. The S 2p spectrum of SACo-MC@MX after Li_2S_6 adsorption (Fig. 3c) revealed the formation of thiosulfate and polythionate, indicating the strong interactions between SACo-MC@MX and Li_2S_6 [51]. The Ti 2p spectrum (Fig. 3d) shows that the peaks all shifted to lower binding energies, demonstrating an increase in the electron density of Ti metal centers due to the interactions between Ti and sulfur [33]. Thus, these results confirm that the SACo-MC@MX not only physically adsorbs LiPSs via its abundant mesoporous structure but also chemically anchors them, effectively suppressing the shuttle effect. To study the catalytic effect of different samples on LiPSs, cyclic voltammetry (CV) tests of symmetrical cells were performed. As shown in Fig. 3e, the CV curve of the SACo-MC@MX electrode displays four distinct redox peaks with lower polarization and higher current response compared to the MC@MX electrode, indicating reduced activation energy for the multistep conversion of polysulfides [52]. Even at an increasing scan rates ranging from 10 to 100 mV s^{-1} (Fig. 3f), the SACo-MC@MX symmetrical cell remain distinct redox peaks with high peak current, indicating that the multistep sulfur conversion reactions proceed smoothly despite intense electron transfer. In contrast, the MC@MX symmetrical cell exhibits flattened under high scan rates (Fig. S5), with indistinguishable peaks, suggesting the active sulfur species are unable to complete the full conversion reaction. The rapid ion and electron transfer is further evidenced by the electrochemical impedance spectroscopy (EIS) results (Fig. 3g). The semicircle in the mid-frequency region represents the charge transfer resistance (R_{ct}) during electrode reactions, which characterizes the rate of charge transfer during the charging and discharging processes [53]. The SACo-MC@MX cell exhibits a smaller semicircle, indicating a lower charge transfer resistance than MC@MX cell. This is consistent with the higher peak current in the CV curves, providing further evidence that Co single atoms facilitate faster charge transfer, thereby accelerating the catalytic conversion of LiPSs. These results further confirm that the introduction of Co single atoms enhances the reaction kinetics of LiPSs.

To further validate the catalytic role of Co single atoms on the nucleation behavior of Li_2S, the potentiostatic discharge experiments were conducted (Fig. 3h–i). The SACo-MC@MX electrode reaches the peak current at 1031 s, significantly earlier than the MC@MX electrode (2140 s). Additionally, the SACo-MC@MX electrode exhibits a larger peak current and a sharper nucleation peak profile for Li_2S. These characteristics suggest that Li_2S nucleation on SACo-MC@MX occurs with lower overpotential, faster response, and higher reaction activity. Furthermore, the deposition capacity of the SACo-MC@MX electrode is 318.5 mAh g^{-1}, higher than that of the MC@MX electrode (245.6 mAh g^{-1}), confirming that SACo-MC@MX promotes the reduction of polysulfides to Li_2S.

CV curves of Li–S cell were used to study the catalytic effects of different materials on the redox reactions. As shown in Fig. 4a, at a scan rate of 0.1 mV s^{-1}, both SACo-MC@MX and MC@MX cells exhibit two sharp reduction peaks near 2.3 V (Peak A) and 2.05 V (Peak B),

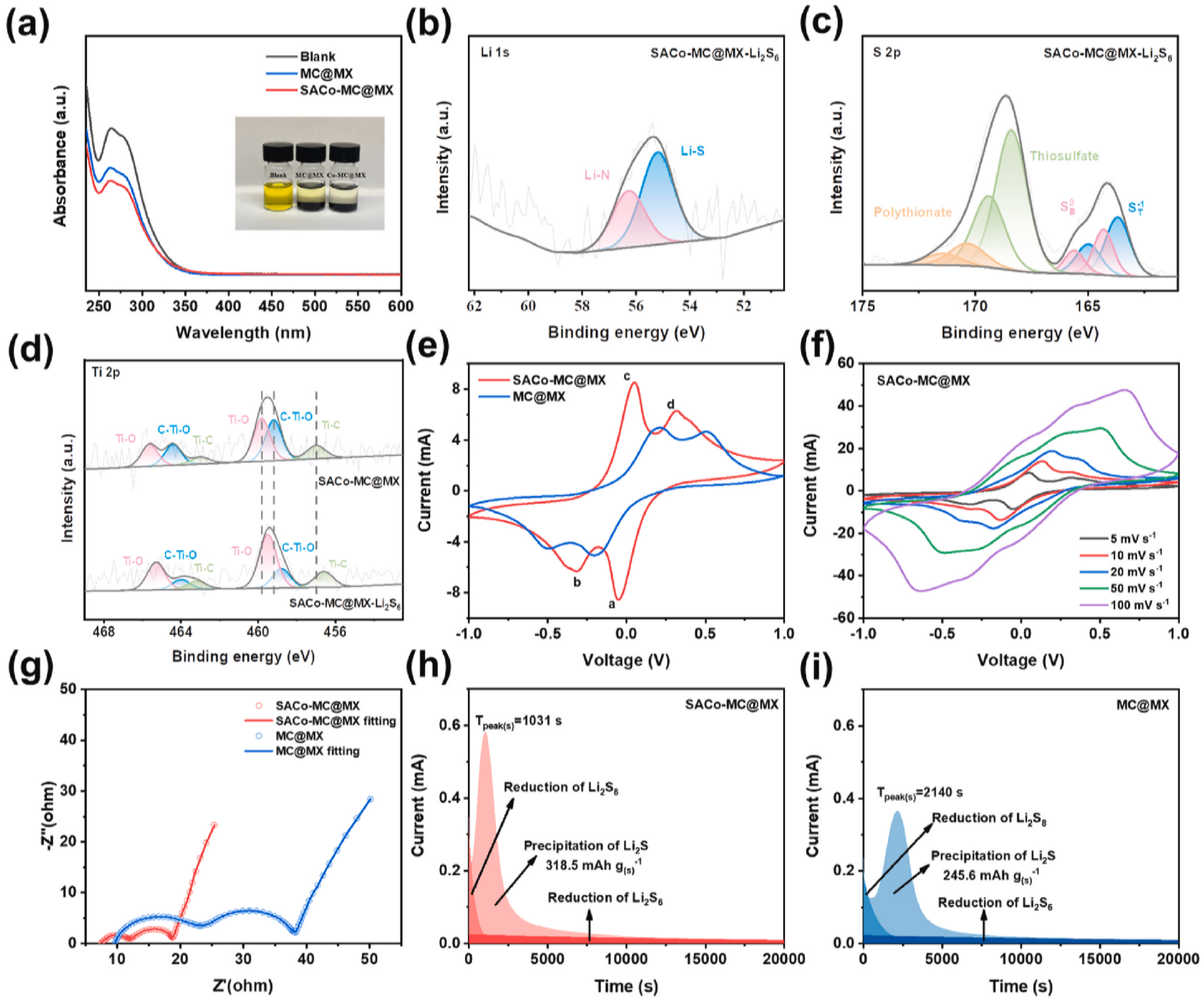

Fig. 3. (A) UV–vis curves of the SACo-MC@MX and MC@MX samples in Li_2S_6 solution. (b) Li 1s, (c) S 2p, and (d) Ti 2p XPS spectra of the SACo-MC@MX sample after Li_2S_6 adsorption. (e) CV curves of symmetric cells with different samples at 5 mv s^{-1}. (f) CV curves of SACo-MC@MX symmetric cells at different scan rates. (g) EIS curves of symmetric cells with different samples. (h, i) Potentiostatic discharge profiles of Li_2S_8 solution with different electrodes.

corresponding to the reduction of S_8 to long-chain LiPSs and the reduction of long-chain LiPSs to Li_2S. A sharp oxidation peak (Peak C) near 2.4 V corresponds to the oxidation of Li_2S to long-chain LiPSs and elemental sulfur [54]. Compared to the MC@MX cell, the SACo-MC@MX cell displays higher reduction potentials and lower oxidation potentials, demonstrating stronger electrochemical driving forces and enhanced sulfur conversion kinetics. This results in significantly reduced polarization behavior. Additionally, the higher current response at the redox peaks of the SACo-MC@MX cell indicates greater electrochemical reactivity and reaction rates, attributed to the enhanced reaction kinetics enabled by Co single atoms. Tafel slopes were calculated for the reduction (Peak B) and oxidation (Peak C) peaks based on the CV curves (Fig. 4b–c). The Tafel slope of the SACo-MC@MX cell for Peak B (42.4 mV dec ^{1}) is smaller than that of the MC@MX cell (58.6 mV dec ^{1}), indicating that the SACo-MC@MX enhances the electrochemical kinetics of the sulfur reduction process and accelerates Li_2S deposition. For Peak C, the SACo-MC@MX cell also exhibits a smaller Tafel slope (78.6 mV dec ^{1}) compared to the MC@MX cell (108.5 mV dec ^{1}), highlighting the electrocatalytic role of SACo-MC@MX in the oxidation of Li_2S to LiPSs. This bidirectional enhancement accelerates the redox reactions in Li–S batteries.

The Li^+ diffusion properties were further evaluated through CV tests at various scan rates. As shown in Figs. 4d and S6a, the CV curves of both cells retain sharp redox peaks as the scan rate increases, with corresponding current responses also increasing, demonstrating good electrochemical stability. Even at 0.5 mV s ^{1}, the SACo-MC@MX cell maintains lower polarization potentials and higher response currents. According to the Randles-Sevcik equation, the Li^+ diffusion kinetics can be evaluated by the slope of the linear relationship between the peak current and the square root of the scanning rate. A smaller slope corresponds to faster Li^+ diffusion [55]. As shown in Figs. 4e and S6b, the SACo-MC@MX cell exhibits higher slopes for Peaks A, B, and C compared to the MC@MX cell, indicating faster Li^+ diffusion rates during the charge and discharge process. This demonstrates that Co single atoms improve the catalytic conversion of LiPSs, reduces their dissolution in the electrolyte, lowers the viscosity of the electrolyte, and accelerates lithium-ion transport.

The Li–S cells were assembled using Li anode and KB/S cathode to evaluate the electrochemical performance with various modified separators. As shown in Fig. 4f, the initial discharge capacity of the SACo-

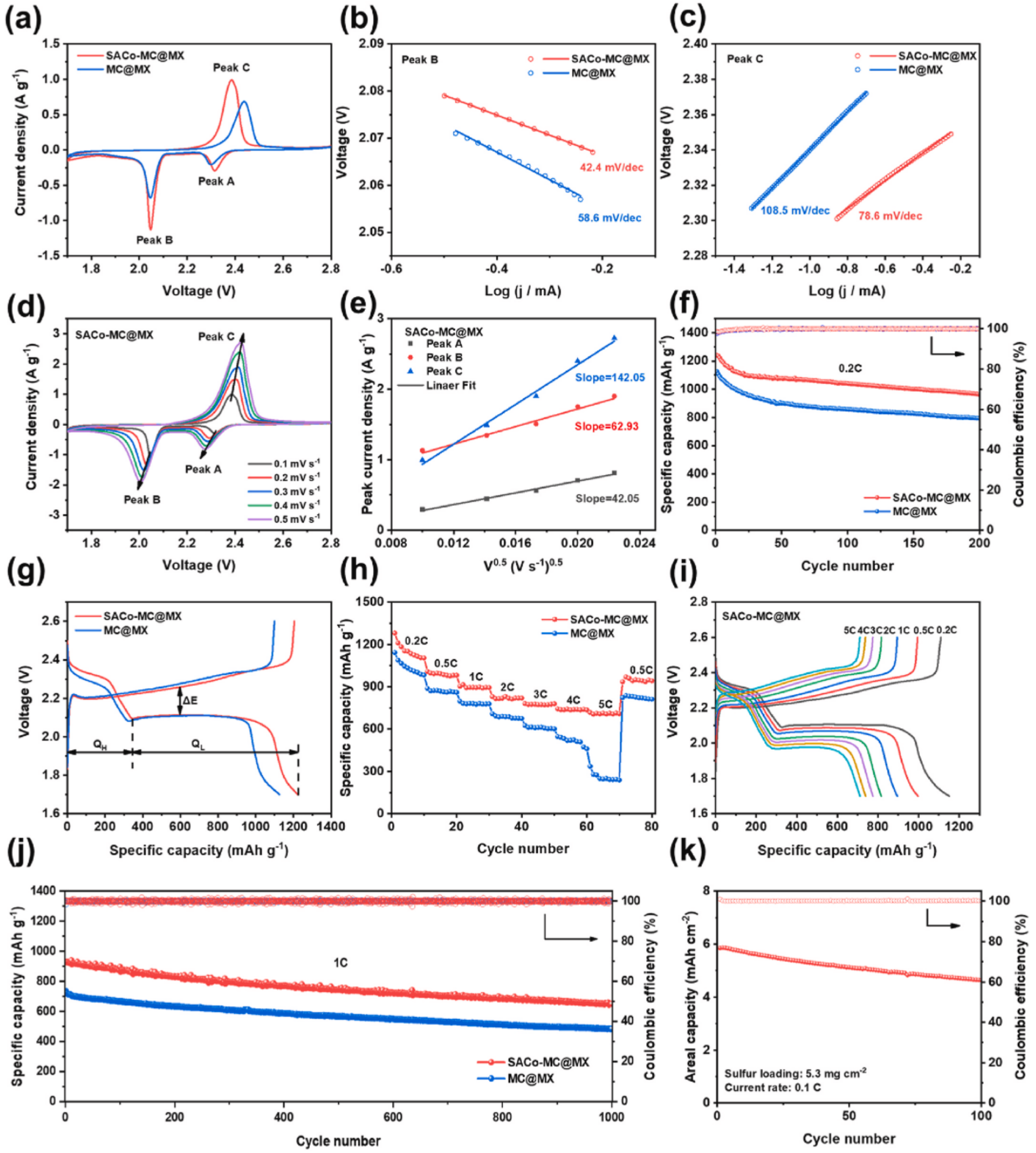

Fig. 4. (A) CV curves and (b, c) derived Tafel curves of SACo-MC@MX and MC@MX. (d) CV curves at different scan rates and (e) peak current fitting curve of SACo-MC@MX. (f) Cycling performance and (g) corresponding charge-discharge profiles at 0.2C, (h) Rate performance and (i) corresponding charge-discharge profiles, (j) Long-term cycle performance at 1C of SACo-MC@MX and MC@MX. (k) Cycling performance at high sulfur loading of SACo-MC@MX.

MC@MX cell is 1241.6 mAh g ^{1}, higher than that of the MC@MX cell (1125.7 mAh g ^{1}), indicating that SACo-MC@MX effectively accelerates the reduction of LiPSs to Li_2S. After 200 cycles, the SACo-MC@MX cell retains a reversible capacity of 965.5 mAh g ^{1} with a capacity retention rate of 77.76 %, superior to the MC@MX cell (794.4 mAh g ^{1}, 70.57 %), demonstrating higher sulfur utilization and cycle stability. Fig. 4g presents the initial charge-discharge curves at 0.2C. Both cells display two discharge plateaus near 2.3 and 2.1 V and one charge plateau near 2.2 V, corresponding to the solid-liquid reduction of sulfur to Li_2S_8, the liquid-solid reduction of short-chain LiPSs to Li_2S, and the oxidation of LiPSs to solid sulfur [56]. The polarization potential of the SACo-MC@MX cell (145 mV) is smaller than that of the MC@MX cell (187 mV), consistent with the CV results, further confirming the SACo-MC@MX separator enhances sulfur redox kinetics. The Q_H/Q_L ratio was calculated to evaluate the catalytic activity of the materials for LiPSs. A higher Q_H/Q_L ratio indicates higher catalytic activity and sulfur utilization during charge and discharge. The SACo-MC@MX cell exhibits a Q_H/Q_L ratio of 2.51, higher than the MC@MX cell (2.44), confirming that SACo-MC@MX accelerates the reduction of LiPSs to Li_2S.

The rate performance of the Li–S cells was tested to evaluate the sulfur redox behavior and reversible capacity at various current rates. As shown in Fig. 4h, the SACo-MC@MX cell achieves capacities of 1280.7, 1008.8, 903.8, 830.0, 780.6, 743.3, and 716.7 mAh g^{-1} at 0.2, 0.5, 1, 2, 3, 4, and 5C, respectively. In comparison, the MC@MX cell keeps capacities of 1142.9, 888.9, 796.8, 708.3, 625.1, 547.0, and 335.9 mAh g^{-1} under the same conditions. The SACo-MC@MX cell consistently delivers higher capacities at all current rates, with the gap widening as the current rate increases, highlighting its superior electrocatalytic capability. When returns to 0.5C, the SACo-MC@MX cell recovers a reversible capacity of 949.2 mAh g^{-1}, demonstrating stable performance even after high-current cycling. Figs. 4i and S7 show the charge-discharge curves of SACo-MC@MX and MC@MX at different current rates. As the current rate increases, the cells' potential polarization also increases due to faster charge transfer at the electrode surface, leading to incomplete charging and discharging. At 5C, the SACo-MC@MX cell maintains a discharge voltage platform around 1.97 V with less polarization, indicating strong catalytic activity and efficient redox reactions even at high current rates. In contrast, the MC@MX cell loses its discharge platform at 5C, with a sharp decrease in capacity due to low LiPS reactivity and concentration polarization. This demonstrates that SACo-MC@MX has stronger catalytic activity, and Co single atoms enhance the sulfur redox kinetics, accelerating the reaction and reducing polarization. To evaluate the suppression of the shuttle effect, long-cycle tests were conducted at a current rate of 1C. As shown in Fig. 4j, the SACo-MC@MX cell also demonstrates excellent long-term cycling stability at 1C after 1000 cycles with a capacity retention rate of 69.9 % (0.030 % capacity decay per cycle) and high Coulombic efficiency approximately 100 %. In contrast, the MC@MX cell only achieves a lower capacity retention rate of 65.8 % (0.034 % capacity decay per cycle). Moreover, even with a high sulfur loading of 5.3 mg cm^{-2}, the cell retains a superior areal capacity of 4.64 mAh cm^{-2} after 100 cycles (Fig. 4k). The outstanding electrochemical performance of the SACo-MC@MX cell can be attributed to the mesoporous carbon structure and Co single atoms, which provides abundant physical adsorption and chemical anchoring sites as well as strong catalytic conversion capability for LiPSs, thus efficiently suppressing the shuttle effect and enabling fast sulfur conversion.

To further confirm the suppression of the lithium polysulfide shuttle effect by SACo-MC@MX, in-situ Raman spectroscopy was performed. As shown in Fig. 5a–b, characteristic peaks of Li_2S_6 (400 cm^{-1}), and liquid electrolyte and Li_2S_8 (LE + S_8^{2-}) (480 cm^{-1}) were detected on the PP separator during the initial discharge stage at 2.32 V [57]. When discharged to 2.11 V, characteristic peaks of Li_2S_4 (200 and 450 cm^{-1}) also appeared, and with further discharge, Li_2S_6 and Li_2S_4 accumulated continuously [58]. These results indicate the occurrence of substantial shuttle behavior on the PP separator, leading to active material loss. In sharp contrast, only the characteristic peak at 480 cm^{-1} corresponding to LE + S_8^{2-} was observed on the SACo-MC@MX modified separator (Fig. 5c–d), demonstrating that SACo-MC@MX, through its combined physical adsorption and chemical anchoring effects, effectively captured polysulfides and significantly suppressed the shuttle effect.

4. Conclusion

In summary, sandwich-like 2D mesoporous carbon/MXene heterostructure integrated with the atomically distributed Co is achieved by single-micelle-directed interfacial assembly strategy, which serves as the bifunctional redox catalyst to propel the sulfur conversions in Li–S

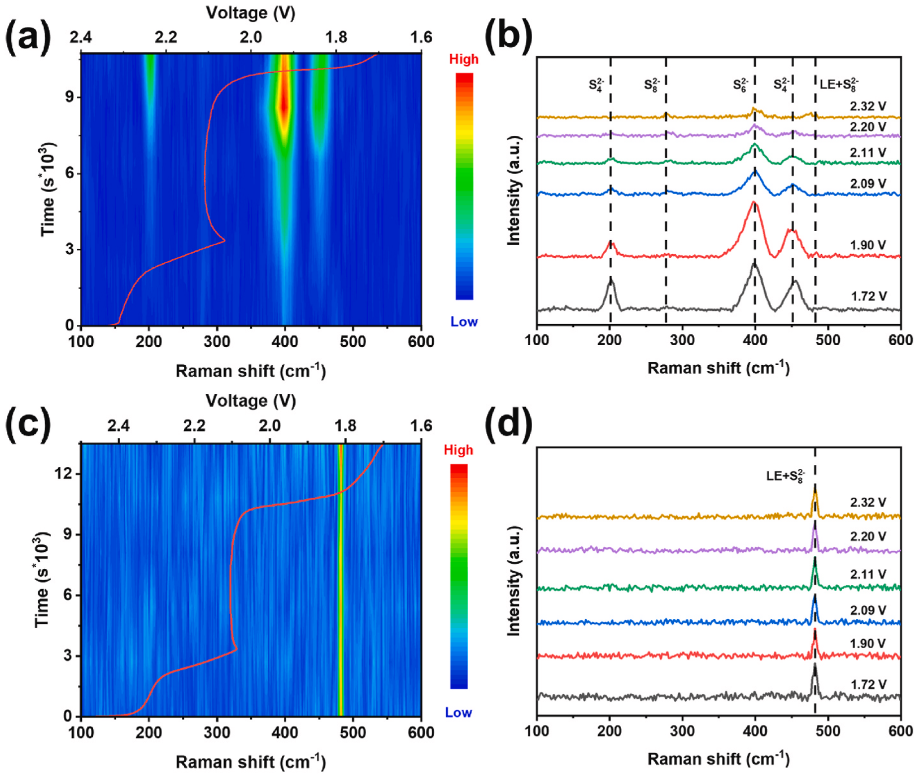

Fig. 5. In situ time-resolved Raman spectra tested during the discharging processes of the cells with (a) PP and (c) SACo-MC@MX. Partial Raman spectra of the cells with (b) PP and (d) SACo-MC@MX.

battery, exhibiting the strategy of "adsorption-catalysis-transformation". Experimental results demonstrate that mesoporous carbon was uniformly grafted onto both sides of MXene, effectively preventing MXene restacking and providing a robust framework for efficient electron and ion transfer. The abundant mesoporous structure not only exposes the Lewis acidic surface of MXene but also maximizes the synergistic effects of heterointerfacial interactions. Furthermore, the Co single atoms exhibit strong catalytic activity, accelerating the catalytic conversion of polysulfides, as confirmed by the in-situ Raman characterization. As a result, Li–S cells with SACo-MC@MX exhibit excellent rate capability up to 5C and outstanding long-cycle performance over 1000 cycles at 1C. Furthermore, even with a high sulfur loading of 5.3 mg cm^{-2}, the cell retains the areal capacity of 4.63 mAh cm^{-2} after 100 cycles, providing new insights for future designs of advanced energy storage systems.

CRediT authorship contribution statement

Jiaheng Bao: Writing – original draft, Formal analysis, Data curation, Conceptualization. **Xiang Li:** Methodology. **Tao Rong:** Validation. **Jian Wang:** Formal analysis. **Jianan Gu:** Resources. **Xiaomin Cheng:** Project administration. **Yanli Wang:** Supervision, Resources. **Hongzhen Lin:** Methodology. **Liang Cheng:** Resources. **Liang Zhan:** Supervision, Funding acquisition. **Yongzheng Zhang:** Writing – review & editing, Supervision, Resources.

Declaration of competing interest

The authors declare that they have no known competing financial interests or personal relationships that could have appeared to influence the work reported in this paper.

Acknowledgments

Dr. Jian Wang thanks the fellowship support from Alexander von Humboldt Foundation. This work is supported by the funding from the National Natural Science Foundation of China (52372045, 22075081, 22279161, and U1710252), National Key R&D Program of China (2021YFA1201503), Shanghai Sailing Program of China (23YF1408900), Natural Science Foundation of Jiangsu Province (BK. 20210130), China Postdoctoral Science Foundation (2023M731084) as well as the Opening funding from Key Laboratory of Engineering Dielectrics and Its Application (Harbin University of Science and Technology) (No. KFM202507, Ministry of Education) are acknowledged. The author thanks the scientific support from Nano-X, Suzhou Institute of Nano-Tech and Nano-Bionics, Chinese Academy of Sciences.

References

[1] Y. Zhang, K. Nie, L. Yi, B. Li, Y. Yuan, Z. Liu, W. Huang, Recent advances in engineering of 2D materials-based heterostructures for electrochemical energy conversion, Adv. Sci. 10 (31) (2023) 2302301.

[2] M. Waqas, Y. Niu, M. Tang, Y. Pang, S. Ali, Y. Dong, W. Lv, W. He, A decade of development in cathode-facing surface modified separators for high-performance Li-S batteries, Energy Storage Mater. 72 (2024) 103682.

[3] Q. Zhao, Q. Zhu, Y. Liu, B. Xu, Status and prospects of MXene-based lithium–sulfur batteries, Adv. Funct. Mater. 31 (21) (2021) 2100457.

[4] Y. Kong, X. Qiu, Y. Xue, G. Li, L. Qi, W. Yang, T. Liu, Y. Li, Sulfonic acid-functionalized graphdiyne for effective Li–S battery separators, J. Am. Chem. Soc. 146 (34) (2024) 23764–23774.

[5] L. Yang, X. Wang, X. Cheng, Y. Zhang, C. Ma, Y. Zhang, J. Wang, W. Qiao, L. Ling, Regulating Fe aggregation state via unique Fe-N-V pre-coordination to optimize the adsorption-catalysis effect in high-performance lithium-sulfur batteries, Adv. Funct. Mater. 33 (38) (2023) 2303705.

[6] Y. Zhang, R. Wang, W. Tang, L. Zhan, S. Zhao, Q. Kang, Y. Wang, S. Yang, Efficient polysulfide barrier of a graphene aerogel–carbon nanofibers–Ni network for high-energy-density lithium–sulfur batteries with ultrahigh sulfur content, J. Mater. Chem. A 6 (42) (2018) 20926–20938.

[7] G. Cao, R. Duan, X. Li, Controllable catalysis behavior for high performance lithium sulfur batteries: from kinetics to strategies, Energy (Calg.) 5 (1) (2023) 100096.

[8] X. Wang, L. Chen, Y. Yu, W. Wang, L. Yue, Z. Shao, H. Wu, Y. Li, Tuning p-band centers and interfacial built-in electric field of heterostructure catalysts to expedite bidirectional sulfur redox for high-performance Li–S batteries, Adv. Funct. Mater. 34 (41) (2024) 2406290.

[9] G. Cai, H. Lv, G. Zhang, D. Liu, J. Zhang, J. Zhu, J. Xu, X. Kong, S. Jin, X. Wu, H. Ji, A volcano correlation between catalytic activity for sulfur reduction reaction and Fe atom count in metal center, J. Am. Chem. Soc. 146 (19) (2024) 13055–13065.

[10] H. Xu, R. Hu, Y. Zhang, H. Yan, Q. Zhu, J. Shang, S. Yang, B. Li, Nano high-entropy alloy with strong affinity driving fast polysulfide conversion towards stable lithium sulfur batteries, Energy Storage Mater. 43 (2021) 212–220.

[11] S. Yu, W. Cai, L. Chen, L. Song, Y. Song, Recent advances of metal phosphides for Li–S chemistry, J. Energy Chem. 55 (2021) 533–548.

[12] C. Cheng, G. Ao, T. Wang, J. Liu, Z. Guan, T. Tao, J. Zhu, Heterostructured MoO2@rGO facilitates enhanced kinetics in lithium-sulfur battery, Carbon 233 (2025) 119897.

[13] C. Cheng, T. Wang, J. Liu, Z. Guan, T. Tao, Y. Yan, J. Zhu, DMSO/DMF co-solvent precipitated nano-sulfur cathode for highly loading lithium-sulfur pouch cells, Chem. Eng. J. 497 (2024) 154785.

[14] Z. Li, G. Liang, T. Wang, J. Liu, C. Cheng, G. Ao, Z. Guan, T. Tao, J. Zhu, Sulfur nanosheets deposited on reduced graphene oxide enable excellent cycling life for lithium-sulfur battery, Carbon 229 (2024) 119512.

[15] X. Wu, R. Xie, D. Cai, B. Fei, C. Zhang, Q. Chen, B. Sa, H. Zhan, Engineering defect-rich bimetallic telluride with dense heterointerfaces for high-performance lithium–sulfur batteries, Adv. Funct. Mater. 34 (26) (2024) 2315012.

[16] J. Xu, W. Tang, C. Yang, I. Manke, N. Chen, F. Lai, T. Xu, S. An, H. Liu, Z. Zhang, Y. Cao, N. Wang, S. Zhao, D. Niu, R. Chen, A highly conductive COF@CNT electrocatalyst boosting polysulfide conversion for Li–S chemistry, ACS Energy Lett. 6 (9) (2021) 3053–3062.

[17] M. Zhao, P. Tan, D. Cai, Y. Liu, C. Zhang, B. Fei, B. Sa, Q. Chen, H. Zhan, Customizing component regulated dense heterointerfaces for crafting robust lithium-sulfur batteries, Adv. Funct. Mater. 33 (8) (2023) 2211505.

[18] E.V. Karaseva, E.V. Kuzmina, B.-Q. Li, Q. Zhang, V.S. Kolosnitsyn, Effect of the anionic composition of sulfolane based electrolytes on the performances of lithium-sulfur batteries, J. Energy Chem. 95 (2024) 231–240.

[19] Y.-W. Song, L. Shen, N. Yao, S. Feng, Q. Cheng, J. Ma, X. Chen, B.-Q. Li, Q. Zhang, Anion-involved solvation structure of lithium polysulfides in lithium–sulfur batteries, Angew. Chem. Int. Ed. 63 (19) (2024) e202400343.

[20] D.-Y. Wang, W. Wang, F. Li, X. Li, W. Guo, Y. Fu, Nitrogen-rich azoles as trifunctional electrolyte additives for high-performance lithium-sulfur battery, J. Energy Chem. 71 (2022) 572–579.

[21] J. Zhang, C. You, H. Lin, J. Wang, Electrochemical kinetic modulators in lithium–sulfur batteries: from defect-rich catalysts to single atomic catalysts, Energy Environ. Mater. 5 (3) (2022) 731–750.

[22] K. Shi, Y. Sun, Z. Xiong, J. Li, H. Nan, Y. Lin, Z. Wei, Q. Liu, Achieving balanced behavior between polysulfides adsorption and catalytic conversion from heterostructure Fe3C-Fe3P promotor for high-performance lithium-sulfur batteries, Chem. Eng. J. 460 (2023) 141794.

[23] J. Xu, H. Zhang, F. Yu, Y. Cao, M. Liao, X. Dong, Y. Wang, Realizing all-climate Li-S batteries by using a porous sub-nano aromatic framework, Angew. Chem. Int. Ed. 61 (47) (2022) e202211933.

[24] Z. Wang, W. Huang, H. Wu, Y. Wu, K. Shi, J. Li, W. Zhang, Q. Liu, 3d-Orbital high-spin configuration driven from electronic modulation of Fe3O4/FeP heterostructures empowering efficient electrocatalyst for Lithium Sulfur batteries, Adv. Funct. Mater. 34 (49) (2024) 2409303.

[25] X. Zhang, X. Li, Y. Zhang, X. Li, Q. Guan, J. Wang, Z. Zhuang, Q. Zhuang, X. Cheng, H. Liu, J. Zhang, C. Shen, H. Lin, Y. Wang, L. Zhan, L. Ling, Accelerated Li^{+} desolvation for diffusion booster enabling low-temperature sulfur redox kinetics via electrocatalytic carbon-grazfted-CoP porous nanosheets, Adv. Funct. Mater. 33 (36) (2023) 2302624.

[26] Z. Du, Y. Guo, H. Wang, J. Gu, Y. Zhang, Z. Cheng, B. Li, S. Li, S. Yang, High-throughput production of 1T MoS2 monolayers based on controllable conversion of Mo-based MXenes, ACS Nano 15 (12) (2021) 19275–19283.

[27] Z. Du, C. Wu, Y. Chen, Q. Zhu, Y. Cui, H. Wang, Y. Zhang, X. Chen, J. Shang, B. Li, W. Chen, C. Liu, S. Yang, High-Entropy carbonitride MAX phases and their derivative MXenes, Adv. Energy Mater. 12 (6) (2022) 2103228.

[28] A. VahidMohammadi, J. Rosen, Y. Gogotsi, The world of two-dimensional carbides and nitrides (MXenes), Science 372 (6547) (2021) eabf1581.

[29] H. Wang, Z. Cui, S.-A. He, J. Zhu, W. Luo, Q. Liu, R. Zou, Construction of ultrathin layered MXene-TiN heterostructure enabling favorable catalytic ability for high-areal-capacity lithium–sulfur batteries, Nano-Micro Lett. 14 (1) (2022) 189.

[30] X. Li, Y. Zuo, Y. Zhang, J. Wang, Y. Wang, H. Yu, L. Zhan, L. Ling, Z. Du, S. Yang, Controllable sulfurization of MXenes to in-plane multi-heterostructures for efficient sulfur redox kinetics, Adv. Energy Mater. 14 (9) (2024) 2303389.

[31] S. Wu, X. Li, Y. Zhang, Q. Guan, J. Wang, C. Shen, H. Lin, J. Wang, Y. Wang, L. Zhan, L. Ling, Interface engineering of MXene-based heterostructures for lithium-sulfur batteries, Nano Res. 16 (7) (2023) 9158–9178.

[32] Z. Ye, Y. Jiang, L. Li, F. Wu, R. Chen, Self-assembly of 0D–2D heterostructure electrocatalyst from MOF and MXene for boosted lithium polysulfide conversion reaction, Adv. Mater. 33 (33) (2021) 2101204.

[33] X. Li, Q. Guan, Z. Zhuang, Y. Zhang, Y. Lin, J. Wang, C. Shen, H. Lin, Y. Wang, L. Zhan, L. Ling, Ordered mesoporous carbon grafted MXene catalytic heterostructure as Li-ion kinetic pump toward high-efficient sulfur/sulfide conversions for Li–S battery, ACS Nano 17 (2) (2023) 1653–1662.

[34] Z. Liang, J. Shen, X. Xu, F. Li, J. Liu, B. Yuan, Y. Yu, M. Zhu, Advances in the development of single-atom catalysts for high-energy-density lithium–sulfur batteries, Adv. Mater. 34 (30) (2022) 2200102.

[35] L. Yang, Y. Pan, Z. Zhou, Y. Zhang, J. Xu, C. Ma, Y. Zhang, J. Wang, W. Qiao, L. Ling, Vanadium as auxiliary for Fe–V dual-atom electrocatalyst in lithium–sulfur batteries: “3D in 2D” morphology inducer and coordination structure regulator, ACS Nano 17 (17) (2023) 17405–17416.

[36] H. Li, J. Wang, J. Zhang, L. Jia, H. Qu, Q. Guan, H. Zhang, H. Lin, Prospects of single atomic catalysts for dendrite-free alkali metal batteries, Green Chem. 26 (20) (2024) 10366–10382.

[37] J. Wang, J. Zhang, Y. Zhang, H. Li, P. Chen, C. You, M. Liu, H. Lin, S. Passerini, Atom-level tandem catalysis in lithium metal batteries, Adv. Mater. 36 (26) (2024) e2402792.

[38] J. Wang, L. Jia, S. Duan, H. Liu, Q. Xiao, T. Li, H. Fan, K. Feng, J. Yang, Q. Wang, M. Liu, J. Zhong, W. Duan, H. Lin, Y. Zhang, Single atomic cobalt catalyst significantly accelerates lithium ion diffusion in high mass loading Li2S cathode, Energy Storage Mater. 28 (2020) 375–382.

[39] J. Wang, L. Jia, J. Zhong, Q. Xiao, C. Wang, K. Zang, H. Liu, H. Zheng, J. Luo, J. Yang, H. Fan, W. Duan, Y. Wu, H. Lin, Y. Zhang, Single-atom catalyst boosts electrochemical conversion reactions in batteries, Energy Storage Mater. 18 (2019) 246–252.

[40] L. Ren, K. Sun, Y. Wang, A. Kumar, J. Liu, X. Lu, Y. Zhao, Q. Zhu, W. Liu, H. Xu, X. Sun, Tandem catalysis inside double-shelled nanocages with separated and tunable atomic catalyst sites for high performance lithium-sulfur batteries, Adv. Mater. 36 (14) (2024) 2310547.

[41] J. Wang, Y. Zuo, Y. Zhang, C. Ma, Z. Chen, J. Wang, W. Qiao, L. Ling, Defect-rich porous graphitic phase carbon nitride layer grafted MXene as desolvation promoter for efficient sulfur conversion in extremely harsh conditions, J. Colloid Interface Sci. 671 (2024) 692–701.

[42] G. Jiang, N. Zheng, X. Chen, G. Ding, Y. Li, F. Sun, Y. Li, In-situ decoration of MOF-derived carbon on nitrogen-doped ultrathin MXene nanosheets to multifunctionalize separators for stable Li-S batteries, Chem. Eng. J. 373 (2019) 1309–1318.

[43] Y. Ren, B. Wang, H. Liu, H. Wu, H. Bian, Y. Ma, H. Lu, S. Tang, X. Meng, CoP nanocages intercalated MXene nanosheets as a bifunctional mediator for suppressing polysulfide shuttling and dendritic growth in lithium-sulfur batteries, Chem. Eng. J. 450 (2022) 138046.

[44] Z. Gou, H. Qu, H. Liu, Y. Ma, L. Zong, B. Li, C. Xie, Z. Li, W. Li, L. Wang, Coupling of N-doped mesoporous carbon and N-Ti3C2 in 2D sandwiched heterostructure for enhanced oxygen electroreduction, Small 18 (15) (2022) 2106581.

[45] Q. Li, J. Wang, Y. Zhang, C. Ma, J. Wang, W. Qiao, L. Ling, In situ construction of 3D 1T-VS2/V2C heterostructures for enhanced polysulfide trapping and catalytic conversion in lithium-sulfur batteries, J. Colloid Interface Sci. 681 (2025) 106–118.

[46] C. Dong, C. Ma, C. Zhou, Y. Yu, J. Wang, K. Yu, C. Shen, J. Gu, K. Yan, A. Zheng, M. Gong, X. Xu, L. Mai, Engineering d-p orbital hybridization with P, S Co-coordination asymmetric configuration of single atoms toward high-rate and long-cycling lithium–sulfur battery, Adv. Mater. 36 (38) (2024) 2407070.

[47] T. Sun, F. Huang, J. Liu, H. Yu, X. Feng, X. Feng, Y. Yang, H. Shu, F. Zhang, Strengthened d-p orbital-hybridization of single atoms with sulfur species induced bidirectional catalysis for lithium–sulfur batteries, Adv. Funct. Mater. 33 (51) (2023) 2306049.

[48] C. Wei, B. Xi, P. Wang, Y. Liang, Z. Wang, K. Tian, J. Feng, S. Xiong, In situ anchoring ultrafine ZnS nanodots on 2D MXene nanosheets for accelerating polysulfide redox and regulating Li plating, Adv. Mater. 35 (32) (2023) 2303780.

[49] L. Chen, J. Xia, Z. Lai, D. Wu, J. Zhou, S. Chen, X. Meng, Z. Wang, H. Wang, L. Zheng, L. Xu, X.-W. Lv, C.W. Bielawski, J. Geng, Coordinatively unsaturated Co single-atom catalysts enhance the performance of lithium–sulfur batteries by triggering strong d–p orbital hybridization, ACS Nano 18 (45) (2024) 31123–31134.

[50] J. Feng, W. Liu, C. Shi, C. Zhang, X. Zhao, T. Wang, S. Chen, Q. Li, J. Song, Enabling fast diffusion/conversion kinetics by thiourea-induced wrinkled N, S co-doped functional MXene for lithium-sulfur battery, Energy Storage Mater. 67 (2024) 103328.

[51] J. Wang, K. Huang, Q. Li, G. Cheng, Y. Zhang, N. Teng, C. Lian, C. Ma, J. Wang, W. Qiao, L. Ling, Synergistic implementation of efficient adsorption-diffusion-conversion in lithium-sulfur batteries via built-in electric field constructed by transition metal selenides, Chem. Eng. J. 500 (2024) 157004.

[52] J. Xu, A. Zhu, Z. Zheng, Y. Qi, Y. Cheng, Y. Cao, B. Peng, L. Ma, Y. Wang, Building Li–S batteries with enhanced temperature adaptability via a redox-active COF-based barrier-trapping electrocatalyst, J. Energy Chem. 101 (2025) 702–712.

[53] Z. Huang, Y. Liang, Z. Wu, Y. Kong, M. Bai, M. Li, B. Hong, T. Huang, S. Huang, H. Chen, S. Zhang, Multifunctional ultrathin Ti3C2Tx MXene@CuCo2O4/PE separator for ultra-high-energy-density and large-capacity lithium-sulfur pouch cells, Adv. Mater. n/a (n/a) (2024) 2410318.

[54] Y. Lin, W. Tang, S. Wu, Y. Zhang, Z. Kong, C. Shen, Y. Wang, L. Zhan, L. Ling, Alleviating the self-discharge and enhancing the polysulphides conversion kinetics with LaCO3OH nanocrystals decorated hierarchical porous carbon, Chem. Eng. J. 452 (2023) 139091.

[55] M. Chen, S. Zhao, S. Jiang, C. Huang, X. Wang, Z. Yang, K. Xiang, Y. Zhang, Suppressing the polysulfide shuttle effect by heteroatom-doping for high-performance lithium–sulfur batteries, ACS Sustainable Chem. Eng. 6 (6) (2018) 7545–7557.

[56] R. Wang, C. Luo, T. Wang, G. Zhou, Y. Deng, Y. He, Q. Zhang, F. Kang, W. Lv, Q.-H. Yang, Bidirectional catalysts for liquid–solid redox conversion in lithium–sulfur batteries, Adv. Mater. 32 (32) (2020) 2000315.

[57] F. Ma, X. Xiong, Z. Zhang, Y. Wu, D. Chen, H. Yu, Y. Wang, X. Li, W. Li, J. He, Y. Chen, Y. Wu, Interface engineering of heterostructural quantum dots towards high-rate and long-life lithium-sulfur full batteries, Nano Energy 133 (2025) 110445.

[58] K. Chen, Y. Zhu, Z. Huang, B. Han, Q. Xu, X. Fang, J. Xu, Strengthened d–p orbital hybridization on metastable cubic Mo2C for highly stable lithium–sulfur batteries, ACS Nano 18 (51) (2024) 34791–34802.